Dalton Transactions

ROYAL SOCIETY OF CHEMISTRY

PAPER

View Article Online
View Journal | View Issue

Check for updates

Cite this: *Dalton Trans.*, 2025, **54**, 15169

A mixed-anion compound based upon a $[Pb_4O_4]$ heterocubane unit: synthesis, structure and electronic properties of $Pb_8O_4I_6(CN_2)$

Albert T. Schwarz,[a] Nele Petersen,[c] Markus Ströbele,[a] David Enseling,[b] Thomas Jüstel,[b] Adam Slabon[c] and H.-Jürgen Meyer*[a]

Received 19th August 2025,
Accepted 8th September 2025

DOI: 10.1039/d5dt01979f

rsc.li/dalton

The present study reports the synthesis, crystal structure, and electronic properties of the lead–oxide–iodide–carbodiimde $Pb_8O_4I_6(CN_2)$. The n-type semiconducting compound was obtained *via* ceramic method from PbI_2, PbO and $Pb(CN_2)$, yielding an air stable, dark yellow crystalline material. Single-crystal X-ray diffraction revealed the monoclinic space group *C*2/*c* featuring a heterocubane-type $[Pb_4O_4]$ motif interconnected by iodide bridges and $(NCN)^{2-}$ units. The optical properties were characterized by diffuse reflectance UV-Vis spectroscopy, Mott–Schottky analysis, and photoluminescence spectroscopy, providing insights into the electronic structure.

Introduction

Over the past decades, the chemistry of metal dinitridocarbonates—commonly referred to as carbodiimides ($(N{=}C{=}N)^{2-}$) or cyanamides ($(N{-}C{\equiv}N)^{2-}$)—has become a dynamic field in solid-state chemistry. This interest is driven by the discovery of structurally diverse compounds exhibiting notable luminescent,[1–6] magnetic,[7–10] and electronic properties.[11–13] Due to their isolobal relationship with chalcogenide anions (O^{2-}, S^{2-}), dinitridocarbonate units can be considered to replace oxide and sulfide anions, enabling the rational design of carbodiimide or cyanamide-based analogues of established oxide and sulfide structures. The electron distribution within the $(NCN)^{2-}$ unit is strongly influenced by the nature and arrangements of surrounding metal atoms. The carbodiimide shape is preferred by hard cations, while the cyanamide form is typically stabilized by softer cations, as anticipated by Pearson's HSAB concept.[14] Dinitridocarbonates based on group 14 elements—including silicon, germanium, tin, and lead—display a wide range of structural patterns and functional properties. These compounds often form extended frameworks composed of tetrahedral or octahedral coordination polyhedra, with the $(NCN)^{2-}$ ligand connecting multiple metal centres.[15–18] Tetracyanamidometallates of the type $[M(CN_2)_4]^{n-}$ (M = Si, Ge) resemble a tetrahedral environment of M atoms, as can be derived from the orthosilicate ion. These compounds are notable for their pronounced photoluminescent properties, second-harmonic generation (SHG) activity, and exceptional thermal as well as hydrolytic stability.[19–23] Tin-based carbodiimides such as $Sn(CN_2)$ and $Sn_2O(CN_2)$ exhibit semiconducting behavior with band gaps near 2.0 eV, and have been investigated as potential materials for energy storage applications, including as electrodes in conversion-type batteries.[24–26] Lead-based carbodiimides display even greater structural complexity. Compounds such as $Pb(CN_2)$, $APb_2Cl_3(CN_2)$ (A = Li, Na, Ag) form extended three-dimensional frameworks consisting of Pb-polyhedra—ranging from trigonal bipyramids and octahedral to more complex arrangements—interconnected by halide and carbodiimide ligands.[1,27,28] In $Pb_7I_6(CN_2)_4$, several Pb-based structural motifs coexist within a layered crystal structure, giving rise to semiconducting behavior with an indirect optical band gap of approximately 2.4 eV. Furthermore, this compound exhibits green photoluminescence at 77 K. Such mixed-anion compounds provide an additional degree of freedom in materials design. In a recent review, Kageyama *et al.* summarized the progress on the synthesis and electronic structure for this class of compounds.[29] Interestingly, the $6s^2$ lone-pair of Pb^{2+} in many carbodiimide-containing compounds appears to be stereochemical inactive or structurally suppressed. By contrast, the influence of the $6s^2$ lone pair becomes prominent in Pb–O-based cluster-like or oxide halide compounds,[30] where low coordination numbers allow its expression. In such systems, Pb^{2+} often adopts pyramidal $[PbO_3]$ coordination, resulting in distinct distortions from ideal geometries. A characteristic example is the occurrence of heterocubane-type $[Pb_4O_4]$ units

[a]*Section for Solid State and Theoretical Inorganic Chemistry, Institute of Inorganic Chemistry, University Tübingen, Auf der Morgenstelle 18, 72076 Tübingen, Germany. E-mail: juergen.meyer@uni-tuebingen.de*
[b]*Department of Chemical Engineering, FH Münster University of Applied Science, Stegerwaldstraße 39, 48565 Steinfurt, Germany*
[c]*Chair of Inorganic Chemistry, University of Wuppertal, Gaußstraße 20, 42119 Wuppertal, Germany*

—comprised of four Pb^{2+} cations and four bridging oxide ions —found in various oxide halides. These building units, characterized by pseudo-tetrahedral geometries and lone-pair-induced distortions, constitute a structurally versatile motif within Pb^{2+} coordination chemistry. In this context, $Pb_8O_4I_6(CN_2)$ represents the first structurally characterized dinitridocarbonate compound with a heterocubane-type $[Pb_4O_4]$ unit, wherein the stereochemically active $6s^2$ lone pair of Pb^{2+} exerts an influence on the local coordination environment.

Results and discussion

Synthesis of $Pb_8O_4I_6(CN_2)$

Although solid-state metathesis (SSM) reactions involving $Li_2(CN_2)$ or $Na_2(CN_2)$ have proven to be efficient and effective methods for the synthesis of a wide range of dinitridocarbonates,[31] the ceramic method,[32] was employed for the preparation of $Pb_8O_4I_6(CN_2)$. This approach involves the homogenization and mechanical grinding of the starting materials PbI_2, PbO, and $Pb(CN_2)$ in a stoichiometric ratio of 3 : 4 : 1 according to reaction (1). The resulting mixture is then subjected to elevated temperatures, yielding $Pb_8O_4I_6(CN_2)$ as a dark yellow powder in high yield. Minor amounts of elemental lead were detected as a side-phase (Fig. 1). Powder XRD confirmed the compound's stability under ambient air and humidity after five days.

$$3PbI_2 + 4PbO + Pb(CN_2) \rightarrow Pb_8O_4I_6(CN_2) \quad (1)$$

An analysis by energy-dispersive X-ray spectroscopy (EDX) on seven distinct points on different single crystals resulted in a lead to iodine ratio of 8 : 5.92(2), thus confirming the Pb : I ratio of $Pb_8O_4I_6(CN_2)$ determined by single-crystal XRD.

Crystal structure

The crystal structure of $Pb_8O_4I_6(CN_2)$ was solved and refined by single-crystal X-ray diffraction (XRD) with monoclinic space group *C*2/*c*. Some selected crystal structure and refinement data are given in Table 1.

The single-crystal refinement revealed the presence of four crystallographically distinct lead positions with unique environments. As demonstrated in Fig. 2, the lead sites Pb1 and Pb2 are surrounded by three oxygen and two iodine atoms for Pb1, and by three iodine atoms for Pb2. The position of Pb3 represents a surrounding with five iodine atoms, one oxygen atom and one $(NCN)^{2-}$ unit. Moreover, the coordination environment of Pb4 comprises four iodine atoms, one oxygen atom, and one $(NCN)^{2-}$ unit. There is one crystallographic $(NCN)^{2-}$ unit present in the structure, where both nitrogen atoms in the $(NCN)^{2-}$ unit are surrounded by two lead atoms (Pb3 and Pb4) each, including Pb–N bond lengths of d_{Pb3-N} = 2.583(4) Å and d_{Pb4-N} = 2.493(4) Å, which are comparable to corresponding Pb–N distances in related lead compounds $Pb_7I_6(CN_2)_4$,[1] $PbCN_2$,[27] $LiPb_2Cl_3(CN_2)$ and LiPbCl (CN_2).[28] The $(NCN)^{2-}$ unit adopts a nearly linear geometry with an N–C–N angle of 179.4(7)° with an identical C–N bond

Table 1 Selected crystal and structure refinement data for $Pb_8O_4I_6(CN_2)$ measured at 150 K

Empirical formula	$Pb_8O_4I_6(CN_2)$
CCDC code	2389167
Formula weight (g mol^{-1})	2522.95
Wavelength (Mo-K$_\alpha$)	0.71073
Crystal system	Monoclinic
Space group	*C*2/*c*
Unit cell dimensions (Å)	a = 18.8050(5)
	b = 8.13080(1)
	c = 16.1378(4)
	β = 114.053(3)
Volume (Å^3)	2253.21(1)
Z	4
Calculated density (g cm^{-3})	7.437
Absorption coefficient (mm^{-1})	67.772
Final R indices ($I > 2\sigma(I)$)	R_1 = 0.0108, wR_2 = 0.0214
R indices (all data)	R_1 = 0.0113, wR_2 = 0.0215
GooF	1.222

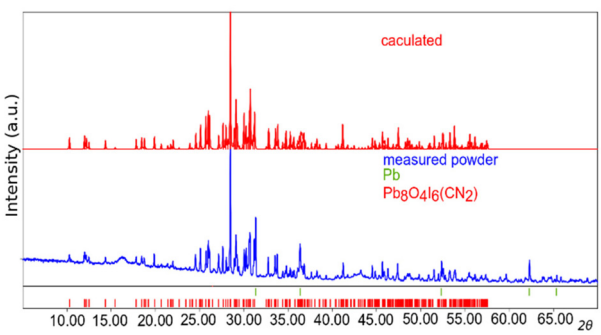

Fig. 1 Recorded powder X-ray diffraction pattern of $Pb_8O_4I_6(CN_2)$ (blue) in comparison with the calculated pattern from the single-crystal refinement (red) and the Bragg positions of the compound (red). Elemental lead appears as a side-phase, shown with its Bragg positions with green color.

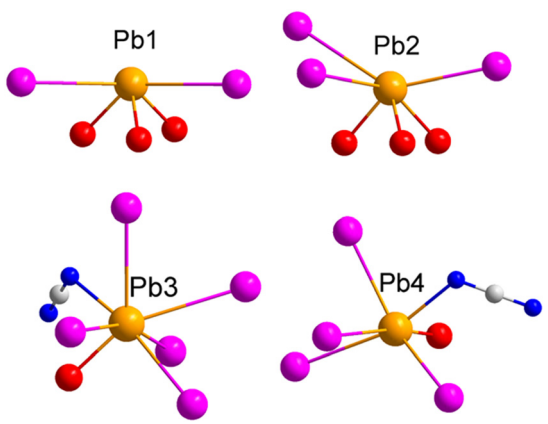

Fig. 2 Coordination environments of four distinct lead positions in $Pb_8O_4I_6(CN_2)$. Iodine atoms are shown in purple, oxygen in red, carbon in white, and nitrogen in blue.

lengths of 1.223(4) Å as a result of a crystallographic twofold rotation axis passing through the central carbon atom. Infrared spectroscopic data (Fig. S1) further confirm the symmetric nature of the carbodiimide unit, revealing the characteristic deformation vibration at 638 cm^{-1} and the asymmetric stretching vibration at 1908 cm^{-1}. A notable feature in the crystal structure of $Pb_8O_4I_6(CN_2)$ is the presence of $[Pb_4O_4]$ unit, resembling the motif of carbon atoms in the cubane structure (C_8H_8) (Fig. 3). In the heterocubane arrangement, each oxygen atom adopts a tetrahedral coordination environment with four lead atoms, including the Pb3 and Pb4 atoms, exhibiting Pb–O bond distances between 2.272(3) Å and 2.382 (3) Å. The Pb positions Pb1 and Pb2 at the corners of the heterocubane adopts pyramidal (PbO_3) geometries, suggesting a localization of the $6s^2$ lone pair of Pb^{2+}. The described Pb–O motif is connected through iodide bridges and $(NCN)^{2-}$ units, with the iodide-bridged heterocubane units being related by a center of symmetry ($\bar{1}$) (Fig. 4 and 5). Such $[Pb_4O_4]$ motifs and coordination patterns have also been observed in lead oxide halide alcoholates[30] and tin oxide halides.[33] In these lead oxide halide alcoholates, however, the heterocubane cores consist of four oxygen atoms, two of which two are from alkoxide groups (OR^-). In contrast, the heterocubane units in $Pb_8O_4I_6(CN_2)$ are composed exclusively of oxide ions.

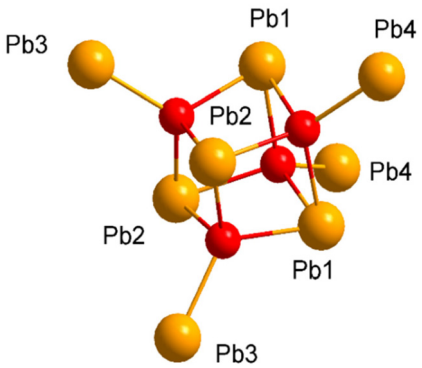

Fig. 3 The heterocubane motif with surrounding lead atoms (Pb3 and Pb4) in the structure of $Pb_8O_4I_6(CN_2)$.

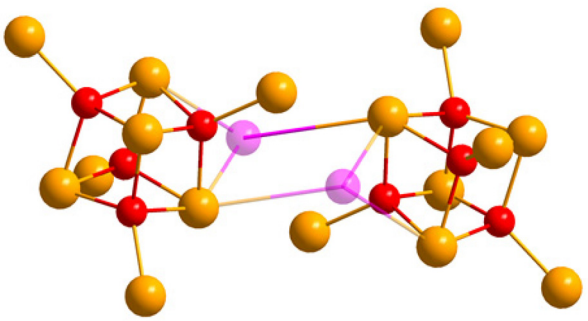

Fig. 4 Section of two iodine-bridged heterocubanes, interconnected by a center of symmetry ($\bar{1}$).

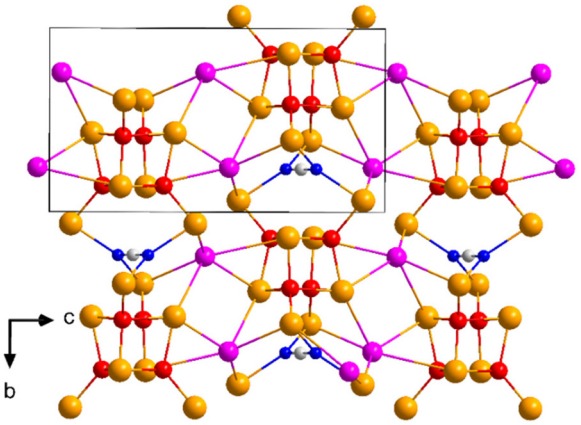

Fig. 5 Representation of the atomic arrangement within a single layer of the $Pb_8O_4I_6(CN_2)$ structure.

Notably, in α-$Pb_6(C_4H_8O_3)O_2I_6$ a comparable arrangement is observed, where the heterocubane units are linked by two diethylene glycolate ligands instead and exhibit an analogous symmetrical relationship ($\bar{1}$). In the aforementioned lead oxide alcoholates, the lead atoms predominantly adopt pyramidal PbO_3 coordination geometries, with an average Pb–O bond length of 2.318 Å, which aligns well with the values observed in $Pb_8O_4I_6(CN_2)$. A comparison of the overall structures of α-$Pb_6(C_4H_8O_3)O_2I_6$ and $Pb_8O_4I_6(CN_2)$ reveals distinct differences in the connectivity of the $[Pb_4O_4]$ units. In the lead alcoholate compound, the $[Pb_4O_4]$ units are arranged in one-dimensional chain-like assemblies that extend into layers within the unit cell. In the crystal structure of $Pb_8O_4I_6(CN_2)$, one type of layer extends within the *bc*-plane and consists of chains running along the *b*-axis, composed of alternating $[Pb_4O_4]$ units and $(NCN)^{2-}$ ligands. Along the *c*-axis, these $[Pb_4O_4]$ units are interconnected by iodide bridges, forming a two-dimensional heterocubane-based network (Fig. 5). Alternating with these layers are planes composed exclusively

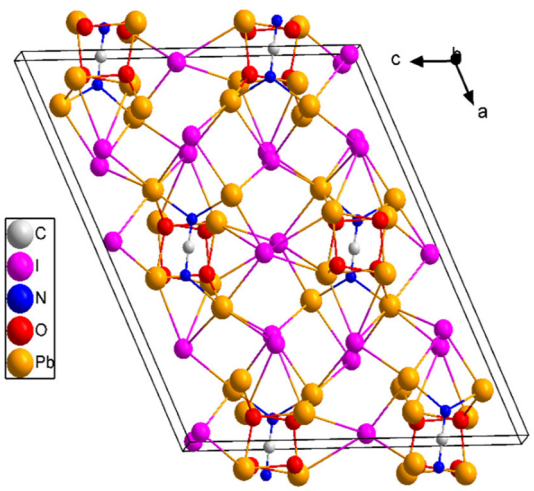

Fig. 6 Unit cell of the compound $Pb_8O_4I_6(CN_2)$.

of iodide ions. Together, these two types of layers stack along the *a*-axis to form the overall layered structure of the compound (Fig. 6). Heterocubane clusters of the type $[Pb_4(OH)_4]^{4+}$ are quite common in aqueous lead(II) chemistry. They appear in the presence of weakly coordinating ligands, for example in $[Pb_4(OH)_4][NO_3]_4$,[34] whereas neutral $[Pb_4O_4]$ species, as in $[Pb_4O_4]Pb_4I_6(CN_2)$ remain less common.

Electronic structure and photoelectrochemistry

In order to determine the band gap of $Pb_8O_4I_6(CN_2)$, the Tauc method was employed in accordance with the following equation:

$$(\alpha \cdot h\nu)^{1/\beta} = A(h\nu - E_g)$$

where α is the absorption coefficient, E_g is the optical band gap, $h\nu$ is the photon energy with the frequency ν, h is the Planck constant, and A is a material-related constant.[35] The Kubelka Munk relation was used to determine the absorption coefficient α.[36] The material exhibits indirect and direct band gaps of 2.58 eV and 2.63 eV, respectively (Fig. S2 and S3). This would render the compound a candidate for use as photoanode in the water oxidation process. Therefore, Mott–Schottky (MS) experiments were conducted to ascertain the semiconducting type and the band edge positions. It is evident from the measured curves (Fig. S4) that they all exhibit a positive slope, thus indicating that $Pb_8O_4I_6(CN_2)$ is an n-type semiconductor. The semiconductor type and the photoactivity was further confirmed by interrupted AM 1.5G illumination (quantum design), as irradiation led to an increase of the measured current density with subsequent decrease to the baseline after switching off the irradiation (Fig. S5). The dark current contribution originates most likely from the photocorrosion, because no passivating layer, *e.g.* amorphous sub-stoichiometric titania, has been applied; a phenomenon known for nitrogen-containing photoanodes.[37,38] The extrapolation of the measured data recorded at 700 Hz yields a flat-band potential of 0.09 V *vs.* reversible hydrogen electrode (RHE) (Fig. 7). For n-type semiconductors, the given potential is close to the conduction band edge (CBE) position. Considering the determined band gaps, the valence band edge (VBE) is positions at 2.67 eV (indirect) and 2.72 eV (direct). The compound exhibits a VBE that is more positive than 1.23 V *vs.* RHE, suggesting its potential as a photoanode for the oxygen evolution reaction (OER).[24,39] The stability of the material under electrochemical conditions was confirmed by cyclic voltammetry before and after the MS measurements. The resulting cyclic voltammogram displays a stable hysteresis, thus confirming the compound's stability (Fig. S6).

Photoluminescence properties

Compounds comprising Pb^{2+} are well known for their intense and long-term stable photoluminescence.[40–44] The high stability of $Pb_8O_4I_6(CN_2)$ in air and against relative humidity, in combination with the straightforward synthesis of the compound, leads to its consideration as a promising material for

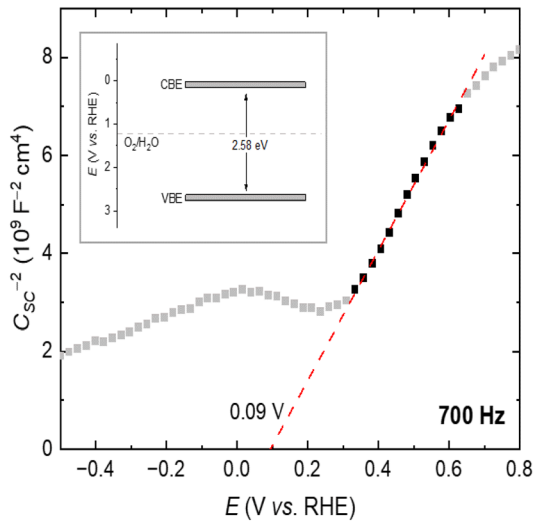

Fig. 7 Mott–Schottky plot of $Pb_8O_4I_6(CN_2)$ on FTO substrate in 0.1 M KPi–electrolyte (Sørensen) with pH 7.0 at a frequency of 700 Hz. Inserted is a schematic representation of the energy levels for $Pb_8O_4I_6(CN_2)$.

application in fluorescent light sources or optical marker. Therefore, an investigation of its photoluminescence properties was carried out.

As demonstrated in Fig. 8, the emission spectrum was observed for the purposes of monitoring the 377 nm excitation at 80 K, resulting in a broad band peaking at 520 nm (19 200 cm^{-1}). The excitation spectrum was observed for monitoring the 520 nm emission at 80 K. As was the case in the preceding research, including the compound $Pb_7I_6(CN_2)_4$,[1] the excitation spectrum is a superposition of three sub-bands peaking at 310 nm (32 300 cm^{-1}), 333 (30 000 cm^{-1}) nm and 376 nm (26 600 cm^{-1}). In order to interpret the excitation and emission spectrum, it is necessary to understand that Pb^{2+} is considered to be an impurity ion of the ns^2 type, with the ground state ($^1S_0$) in the $6s^2$ electronic configuration and the

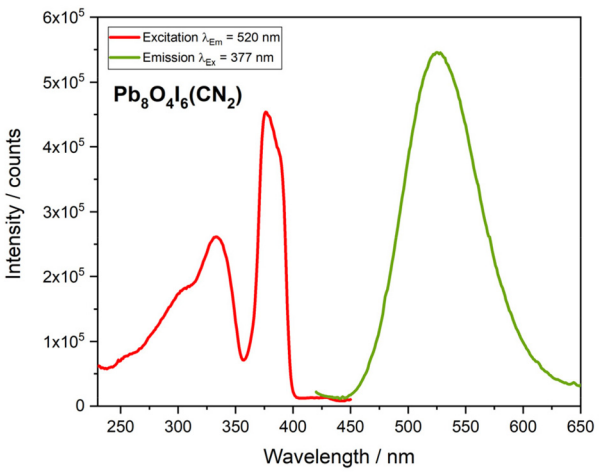

Fig. 8 Excitation and emission spectra of $Pb_8O_4I_6(CN_2)$ at 80 K.

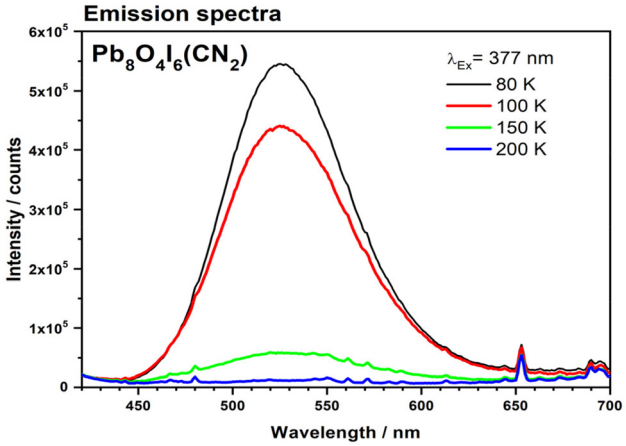

Fig. 9 Temperature dependent emission spectra of $Pb_8O_4I_6(CN_2)$ upon 377 nm excitation between 80 and 200 K.

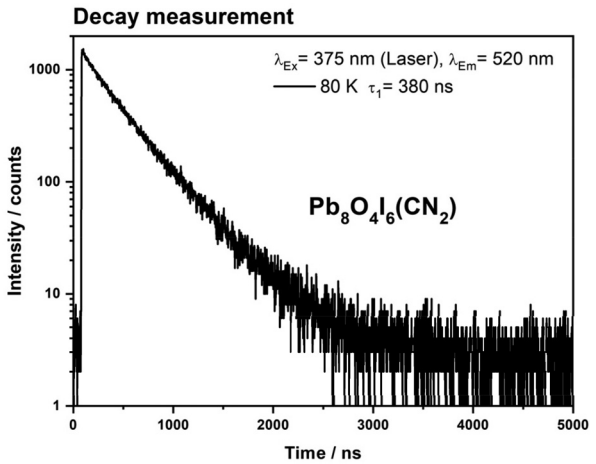

Fig. 10 Decay curve monitored for the 525 nm emission of $Pb_8O_4I_6(CN_2)$ upon 375 nm excitation at 80 K.

first excited state in the $6s^1p^1$ electronic configuration. The first excited state splits into four states consisting of three triplet ($^3P_0$, $^3P_1$, $^3P_2$) and a single state ($^1P_1$). The excitation band observed in the spectrum peaking at 310 nm, 333 nm, and 376 nm can be assigned to the transitions from the ground state $^1S_0$ to the three excited states $^3P_0$, $^3P_1$, $^3P_2$ of Pb^{2+} The emission band can be assigned to the $^3P_1$–$^1S_0$ transition, which is almost completely quenched at 150 K (Fig. 9). The decay curve of the photoluminescence at 80 K (Fig. 10) shows a mono-exponential behavior with a decay time of about $\tau_{1/c}$ = 380 ns.

Conclusions

The reaction between lead cyanamid, lead oxide and lead iodide resulted in the formation of the new $Pb_8O_4I_6(CN_2)$, as confirmed by PXRD and EDX analysis. The compound features a heterocubane-like $[Pb_4O_4]$ motif interconnected *via* iodide bridges and carbodiimide units. The material demonstrates chemical and structural stability under ambient conditions. Optical and electrochemical measurements reveal an indirect band gap of 2.58 eV, a direct band gap of 2.63 eV, and n-type semiconducting behavior with a flat-band potential conducive to water oxidation. Moreover, photoluminescence of $Pb_8O_4I_6(CN_2)$ at low temperatures was confirmed by photoluminescence spectroscopy. The straight forward synthesis and the air-stability of $Pb_8O_4I_6(CN_2)$ emphasize its potential as a photoactive material for photoelectrochemical applications and as a luminescent compound for optical technologies.

Experimental section and calculation details

Preparation of $Pb_8O_4I_6(CN_2)$

Crystalline powders of $PbCN_2$ (synthesized as described in the literature[45]), PbI_2 (purchased from Sigma-Aldrich, 99.999% purity) and PbO (purchased from Sigma-Aldrich, 99.999% purity) were mixed in a glove box under dry argon atmosphere in a 3 : 1 : 4 molar ratio. The reaction mixture was then transferred into a silica ampoule and sealed under vacuum. The ampoule was then heated in a crucible furnace at 420 °C at a heating and cooling rate of 2 K min^{-1} for a duration of five days. The reaction product was obtained as a dark yellowish powder, with an estimated yield of 90%, and elemental lead as a side phase.

Synthesis of $Pb_8O_4I_6(CN_2)$ thin film on FTO

The FTO glass was first thoroughly washed with water and acetone. For EPD, a suspension was prepared by dissolving 20 mg of iodine in 20 mL of acetone. Subsequently, approx. 100 mg of $Pb_8O_4I_6(CN_2)$ powder was added to the solution. The mixture was sonicated for 60 min at room temperature to obtain small particles and ensure homogeneity of the suspension. The EPD cell consisted of FTO glass as conductive substrate connected as the working electrode (negative terminal) and a platinum wire as the counter electrode (positive terminal). The electrodes were positioned parallel to each other at a fixed distance. A voltage of 45 V was applied to the system using a Voltcraft HPS-16010 power supply. The resulting coated FTO glass was gently rinsed with water and acetone to remove loose particles and the electrode was dried at room temperature overnight.

Single-crystal XRD

Single-crystal XRD studies were performed using a Rigaku XtaLab Synergy-S diffractometer with monochromatic Mo-Kα (λ = 0.71073 Å) radiation and a mirror monochromator. Measurements were conducted under N_2 cooling at 150 K. Corrections for absorption effects of the X-ray intensities were applied with a numerical method using CrysAlisPro 1.171.43.121 (Rigaku Oxford Diffraction, 2024).[46] The structure was solved by ShelXT (Sheldrick, 2008)[47] The model was refined with ShelXL 2019/3 (Sheldrick, 2015)[48] using full

matrix least squares implemented in Olex2 1.5-ac5-024 (Dolomanov *et al.*, 2009).[49]

Powder XRD

The powder samples were analysed using an X-ray powder diffractometer (STOE Darmstadt, STADI-P, Ge-monochromator) with Cu-Kα_1 radiation (λ = 154.0598 pm) in the 2θ range between 5° to 70°.

IR-spectroscopy

Infrared spectra were recorded using a VERTEX 70 FT-IR Spectrometer in the range of 400 cm^{-1} to 4000 cm^{-1} using KBr pellets of $Pb_8O_4I_6(CN_2)$. Samples were prepared in a glove-box under Argon atmosphere.

Photoluminescence spectroscopy

Excitation and emission spectra of $Pb_8O_4I_6(CN_2)$ sample were recorded using a fluorescence spectrometer FLS920 (Edinburgh Instruments) equipped with a 450 W xenon discharge lamp (OSRAM) as the radiation source. For powder samples a mirror optic was mounted inside the sample chamber. For the collection of data, a R2658P single-photon-counting photomultiplier tube from Hamamatsu was used. For temperature adjustment a cryostat "MicrostatN" from the company Oxford Instruments had been applied to the present spectrometer. Liquid nitrogen was used as a cooling agent. The photoluminescence decay curve was also measured on the FLS920 spectrometer, while a 375 nm ps laser diode from Edinburgh Instruments was used as an excitation source.

UV-Vis in diffuse reflectance

The reflectance spectra were recorded on an OceanOptics Maya 2000 Pro spectrometer equipped with a Harrick praying mantis sample chamber. A deuterium tungsten lamp (DH 200 BAL) from OceanOptics was used as the light source. The measurement was performed with the following settings: scan to average = 100, boxcar width = 10 and integration time = 300 ms using OceanView 1.6.7 (lite) software from OceanOptics. To determine the optical band gap E_g, the Tauc equation was used: $(\alpha \cdot h\nu)^{1/r} = A(h\nu - E_g)$, where α is the absorption coefficient, h is the Planck constant, A is a material related constant and $h\nu$ is the photon energy. For a direct allowed bandgap transition, r = 1/2, and for an indirect allowed bandgap transition, r = 2.

EDX measurements

The energy dispersive X-ray spectroscopy (EDX) was performed with a Hitachi SU8030 scanning electron microscope equipped with a Bruker QUANTAX 6G EDX detector.

Photoelectrochemistry

Mott–Schottky (MS) measurements were performed with a BioLogic SP-300 potentiostat using a three-electrode setup and floating ground. The prepared electrode was used as working electrode, a platinum wire was used as counter electrode and an Ag/AgCl electrode in saturated KCl was used as reference electrode. The measured potential was recorded *vs.* $E_{Ag/AgCl\ (KCl\ sat.)}$ (V) and then converted to the reversible hydrogen electrode (RHE) E_{RHE} (V) according to E_{RHE} (V) = 0.197 + $E_{Ag|AgCl|KCl\ sat}$ + (0.059·pH) at 25 °C. The measurements were performed in a potassium phosphate buffer (0.1 M KPi) as electrolyte pH 7 in the dark at an AC amplitude of 10 mV with frequencies in the decadic distant range of 0.7 Hz to 700 Hz, to determine the band edge E_{FB}.

Chronoamperometry (CA) was performed at 0 V *vs.* RHE to again determine whether $Pb_8O_4I_6(CN_2)$ exhibits p-type or n-type behaviour by applying an AM 1.5G illumination at 100 mW cm^{-2} to the electrode and interrupting the illumination every 30 seconds for 30 seconds. The measurement was started in the dark.

Capacitance measurement according to the MS function

$$\frac{1}{{C_{sc}}^2} = \frac{2}{A^2 \varepsilon \varepsilon_0 q N_D}\left(E - E_{FB} - \frac{k_b T}{q}\right)$$

In the equation, C_{SC} is determined to be the capacitance in the space-charge-layer, ε is the dielectric constant of the material, A is the interfacial area of electrode and electrolyte, the permittivity of free space is ε_0, q is the electronic charge, N_D is the donor density, E is the potential that is applied, k_b the Boltzmann's constant, T is the absolute temperature, and E_{FB} is the flat-band potential. E_{FB} and $2/(A^2\varepsilon\varepsilon_0 q N_D)$ can be determined using a plot of $1/{C_{SC}}^2$ against E from the x-axis intercept and the slope of the linear region, respectively. The type of semiconductor can be identified by the slope of $2/(A^2\varepsilon\varepsilon_0 q N_D)$ being positive for an n-type or negative for a p-type. The obtained results for E_{FB} correspond approximately to the conducting band edge, E_{CB}, of an n-type or to the valence band edge, E_{VB}, of a p-type semiconductor respectively. When one of the potentials (E_{VB} or E_{CB}) is defined, the respective other potential can be deduced based on $E_g = E_{VB} - E_{CB}$.

Conflicts of interest

The authors declare no conflict of interest.

Data availability

The data that support the findings of this study are available in the SI. Supplementary information is available. See DOI: https://doi.org/10.1039/d5dt01979f.

CCDC 2389167 contains the supplementary crystallographic data for this paper.[50]

Acknowledgements

We gratefully acknowledge the support provided by the Deutsche Forschungsgemeinschaft (DFG-Bonn) for this research project (ME 914/34-1).

References

1 A. T. Schwarz, M. Ströbele, C. P. Romao, D. Enseling, T. Jüstel and H.-J. Meyer, *Dalton Trans.*, 2024, **53**, 6416–6422.
2 D. Dutczak, A. Siai, M. Ströbele, D. Enseling, T. Jüstel and H.-J. Meyer, *Eur. J. Inorg. Chem.*, 2020, **2020**, 3954–3958.
3 C.-D. Brand, M. Ströbele, D. Enseling, T. Jüstel and H.-J. Meyer, *J. Cluster Sci.*, 2024, **35**, 101–107.
4 A. Siai, C.-D. Brand, M. Ströbele, D. Enseling, T. Jüstel and H.-J. Meyer, *J. Cluster Sci.*, 2023, **34**, 1001–1008.
5 Y.-C. Wu, T.-M. Chen, C.-H. Chiu and C.-N. Mo, *J. Electrochem. Soc.*, 2010, **157**, J342.
6 M. Krings, G. Montana, R. Dronskowski and C. Wickleder, *Chem. Mater.*, 2011, **23**, 1694–1699.
7 M. Li, P. Zhang and X. Wei, *J. Phys. Chem. Solids*, 2016, **98**, 123–127.
8 X. Liu, M. Krott, P. Müller, C. Hu, H. Lueken and R. Dronskowski, *Inorg. Chem.*, 2005, **44**, 3001–3003.
9 M. Krott, X. Liu, B. P. T. Fokwa, M. Speldrich, H. Lueken and R. Dronskowski, *Inorg. Chem.*, 2007, **46**, 2204–2207.
10 X. Liu, L. Stork, M. Speldrich, H. Lueken and R. Dronskowski, *Chem. – Eur. J.*, 2009, **15**, 1558–1561.
11 M. Löber, C. S. Geißenhöner, M. Ströbele, S. Indris, C. P. Romao and H.-J. Meyer, *Inorg. Chem.*, 2019, **58**, 14560–14567.
12 X. Qiao, Z. Ma, D. Luo, A. J. Corkett, A. Slabon, A. Rokicinska, P. Kuśtrowski and R. Dronskowski, *Dalton Trans.*, 2020, **49**, 14061–14067.
13 M. Davi, M. Mann, Z. Ma, F. Schrader, A. Drichel, S. Budnyk, A. Rokicinska, P. Kustrowski, R. Dronskowski and A. Slabon, *Langmuir*, 2018, **34**, 3845–3852.
14 R. G. Pearson, *J. Am. Chem. Soc.*, 1963, **85**, 3533–3539.
15 X. Meng, F. Liang, W. Yin, Z. Lin and M. Xia, *New J. Chem.*, 2019, **43**, 9766–9770.
16 R. Riedel, A. Greiner, G. Miehe, W. Dressler, H. Fuess, J. Bill and F. Aldinger, *Angew. Chem., Int. Ed. Engl.*, 1997, **36**, 603–606.
17 M. Kubus, J. Glaser, A. Kłonkowski and H.-J. Meyer, *Z. Anorg. Allg. Chem.*, 2010, **636**, 991–995.
18 M. Löber, M. Ströbele, C. P. Romao and H.-J. Meyer, *Eur. J. Inorg. Chem.*, 2021, **2021**, 4572–4578.
19 K. D. Röseler, K. Eichele, M. Ströbele and H.-J. Meyer, *Eur. J. Inorg. Chem.*, 2024, **27**, 1–6.
20 J. Glaser and H.-J. Meyer, *Angew. Chem.*, 2008, **120**, 7658–7661.
21 K. Dolabdjian, C. Schedel, D. Enseling, T. Jüstel and H.-J. Meyer, *Z. Anorg. Allg. Chem.*, 2017, **643**, 488–494.
22 D. Dutczak, M. Ströbele, D. Enseling, T. Jüstel and H.-J. Meyer, *Eur. J. Inorg. Chem.*, 2016, **2016**, 4011–4016.
23 J. Glaser, H. Bettentrup, T. Jüstel and H.-J. Meyer, *Inorg. Chem.*, 2010, **49**, 2954–2959.
24 Z. Chen, M. Löber, A. Rokicińska, Z. Ma, J. Chen, P. Kuśtrowski, H.-J. Meyer, R. Dronskowski and A. Slabon, *Dalton Trans.*, 2020, **49**, 3450–3456.
25 M. Löber, K. Dolabdjian, M. Ströbele, C. P. Romao and H.-J. Meyer, *Inorg. Chem.*, 2019, **58**, 7845–7851.
26 K. Dolabdjian, A. L. Görne, R. Dronskowski, M. Ströbele and H.-J. Meyer, *Dalton Trans.*, 2018, **47**, 13378–13383.
27 X. Liu, A. Decker, D. Schmitz and R. Dronskowski, *Z. Anorg. Allg. Chem.*, 2000, **626**, 103.
28 K. Dolabdjian and H.-J. Meyer, *Z. Anorg. Allg. Chem.*, 2017, **643**, 1898–1903.
29 H. Kageyama, H. Ogino, T. Zhu and T. Hasegawa, *Mixed-anion Compounds*, Royal Society of Chemistry, 2024.
30 T. Oldag and H.-L. Keller, *Z. Anorg. Allg. Chem.*, 2006, **632**, 1267–1272.
31 H.-J. Meyer, *Dalton Trans.*, 2010, **39**, 5973–5982.
32 C. N. R. Rao and K. Biswas, *Essentials of Inorganic Materials Synthesis*, Wiley, New Jersey, 2015, pp. 17–21.
33 M. Löber, C. S. Geißenhöner, M. Ströbele, C. P. Romao and H.-J. Meyer, *Eur. J. Inorg. Chem.*, 2021, **2021**, 283–288.
34 S. M. Grimes, S. R. Johnston and I. Abrahams, *J. Chem. Soc., Dalton Trans.*, 1995, 2081–2086.
35 P. Makuła, M. Pacia and W. Macyk, *J. Phys. Chem. Lett.*, 2018, **9**, 6814–6817.
36 W. W. Wesley and H. G. Hecht, *Reflectance Spectroscopy*, Wiley, New York, NY, USA, 1966, p. 298.
37 C. Lu, J. Chen, K. Piętak, A. Rokicińska, P. Kuśtrowski, R. Dronskowski, J. Yuan, S. Budnyk, S. Złotnik, R. H. Coridan and A. Slabon, *Chem. Mater.*, 2022, **34**, 6902–6911.
38 Z. Ma, T. Thersleff, A. L. Görne, N. Cordes, Y. Liu, S. Jakobi, A. Rokicinska, Z. G. Schichtl, R. H. Coridan, P. Kustrowski, W. Schnick, R. Dronskowski and A. Slabon, *ACS Appl. Mater. Interfaces*, 2019, **11**, 19077–19086.
39 T. R. Harris-Lee, F. Marken, C. L. Bentley, J. Zhang and A. L. Johnson, *EES Catal.*, 2023, **1**, 832–873.
40 H. Folkerts, M. Hamstra and G. Blasse, *Chem. Phys. Lett.*, 1995, **246**, 135–138.
41 H. F. Folkerts and G. Blasse, *J. Mater. Chem.*, 1995, **5**, 273–276.
42 H. Folkerts and G. Blasse, *Chem. Mater.*, 1994, **6**, 969–972.
43 M. Yılmaz and E. Erdoğmuş, *J. Lumin.*, 2020, **218**, 116868.
44 P. Yang, M. K. Lü, C. F. Song, S. W. Liu, F. Gu and S. F. Wang, *Inorg. Chem. Commun.*, 2004, **7**, 268–270.
45 X. Liu, A. Decker, D. Schmitz and R. Dronskowski, *Z. Anorg. Allg. Chem.*, 2000, **626**, 103–105.
46 *CrysAlisPro Software System*, Rigaku Oxford Diffraction, 2024.
47 G. M. Sheldrick, *Acta Crystallogr., Sect. A: Found. Crystallogr.*, 2008, **64**, 112–122.
48 G. M. Sheldrick, *Acta Crystallogr., Sect. C: Struct. Chem.*, 2015, **71**, 3–8.
49 O. V. Dolomanov, L. J. Bourhis, R. J. Gildea, J. A. K. Howard and H. Puschmann, *J. Appl. Crystallogr.*, 2009, **42**, 339–341.
50 A. T. Schwarz, N. Petersen, M. Ströbele, D. Enseling, T. Jüstel, A. Slabon and H.-J. Meyer, CCDC 2389167: Experimental Crystal Structure Determination, 2025, DOI: **10.5517/ccdc.csd.cc2l63xv**.